# Optical properties of mutant versus wild-type mouse skin measured by reflectance-mode confocal scanning laser microscopy (rCSLM)

**Ravikant Samatham**
**Steven L. Jacques**
Oregon Health & Science University
Department of Biomedical Engineering
3303 SW Bond Avenue
Portland, Oregon 97239
E-mail: sjacques@bme.ogi.edu

**Paul Campagnola**
University of Connecticut Health Center
Center for Biomedical Imaging Technology
Department of Physiology
263 Farmington Avenue
Farmington, Connecticut 06030

**Abstract.** Separation of the two optical scattering properties, the scattering coefficient ($\mu_s$) and the anisotropy of scattering (g), has been experimentally difficult in tissues. A new method for measuring these properties in tissues uses reflectance-mode confocal scanning laser microscopy (rCSLM). Experimentally, the focus at depth $z$ is scanned down into the tissue. The measured data is the exponential decay of the confocal reflectance signal as a function of the depth of the focal volume, $R(z)=\rho \exp(-\mu z)$, summarized as a local reflectivity ($\rho$) and an exponential decay constant ($\mu$). The $\rho$ and $\mu$ map uniquely into the $\mu_s$ and g of the tissue. The method was applied to three mouse skin tissues: one wild-type (wt/wt), one heterozygous mutant (oim/wt), and one homozygous mutant (oim/oim), where oim indicates the mutation for *osteogenesis imperfecta*, a bone disease that affects type I collagen structure. The mutation affects the collagen fibrils of the skin and the assembly of collagen fiber bundles. The anisotropy of scattering (g) at 488 nm wavelength decreased from 0.81 to 0.46 with the added mutant allele. There was a slight increase in the scattering coefficient ($\mu_s$) with the mutation from 74 to 94 $cm^{-1}$. The decrease in g (toward more isotropic scattering) is likely due to the failure of the mutant fibrils to assemble into the larger collagen fiber bundles that yield forward scattering. 
[DOI: 10.1117/1.2953195]

Keywords: reflectance-mode confocal scanning laser microscopy (rCSLM); optical coherence tomography (OCT); scattering coefficient; anisotropy of scattering; osteogenesis imperfecta.

Paper 07402SSRR received Sep. 25, 2007; revised manuscript received Apr. 15, 2008; accepted for publication Apr. 28, 2008; published online Jul. 18, 2008.

## 1 Introduction

Many methods have been developed in the past few decades to determine the optical properties of turbid media, like tissues, that depend on light diffusion. They include diffuse reflectance, diffuse transmission, and reflectance as a function of source-detector distance.[1–3] These techniques can measure the absorption coefficient ($\mu_a$) and the reduced scattering coefficient [$\mu_s'=\mu_s(1-g)$]. But separating $\mu_s'$ into the scattering coefficient ($\mu_s$) and the anisotropy of scattering (g) is difficult unless a tissue sample is removed to allow other measurements, like collimated transmission or goniometry. Knowing both $\mu_s$ and g can characterize the ultrastructure of tissues that yields the scattering properties, i.e., the apparent particle size distribution like mitochondria, nuclei, lipid membranes, collagen, etc. More information from the $\mu_s$ and g of tissues may prove useful in monitoring the changes in ultrastructure due to different pathologies.[4]

In this work, *reflectance-mode confocal scanning laser microscopy* (rCSLM) was used to determine the optical properties of excised murine skin samples. Contrast in rCSLM is due to the scattering by the tissue ultrastructure, which enables noninvasive imaging of tissues without introducing external contrast agents. The collection of reflectance from the focus of a high-numerical-aperture (NA) lens is a function of the scattering properties of the tissue. The rCSLM provides a signature of the tissue-scattering properties that characterizes the ultrastructure. A simple analysis has being developed in our laboratory to extract optical properties ($\mu_s$ and g) from the confocal signal, $R(z)$, obtained as a function of the depth of focus, $z$.[5,6]

Other groups have also studied the use of confocal reflectance, or optical coherence tomography (OCT), which is similar, as a function of the depth of the focus to determine the scattering coefficient $\mu_s^4$ and anisotropy g.[7,8] However, these previous reports have not considered the contribution of photons that partially scatter but still reach the focus. This paper outlines the analysis that considers such photons when interpreting measurements to yield optical properties.

Address all correspondence to: Steven L. Jacques, Department of Biomedical Engineering, Oregon Health & Sciences University, Mail Code: CH 13B, 3303 SW Bond Avenue, Portland, OR 97239. Tel: 503-418-9338; Fax: 503-418-9311; E-mail: sjacques@bme.ogi.edu.

1083-3668/2008/13(4)/041309/7/$25.00 © 2008 SPIE

In this paper, optical measurements are used to sense a single gene defect by its affect on dermal scattering properties in a murine model. The mutation is a dominant negative gene defect that causes *osteogenesis imperfecta*, also called brittle bone disease, which is caused by a defect in type I collagen structure and characterized by brittle bones that are prone to frequent fractures.[9] The gene defect also manifests as a change in dermal scattering due to the failure of collagen fibrils to properly form and assemble into collagen fiber bundles. The structural consequences of this mutation have been studied using second harmonic generation imaging.[10]

## 2 Methods

### 2.1 *Animals*

The optical study was conducted on murine skin samples from the University of Connecticut, where the mice carrying the *osteogenesis imperfecta* mutation were maintained in the B6C3Fe-a/a (C57BL/6JLe X C3HeB/FeJLe) hybrid background under approved animal care protocol. The animals were 3 to 4 months in age. Skin tissues were harvested from the thigh area immediately after euthanasia, then placed in saline and packed in ice for shipping. Samples were received at the Oregon Health & Science University within 24 hours, and optical experiments were conducted immediately.

The three skin tissue samples were blindly labeled as #1, #2, and #3, and later revealed to be:

$$\#1 = \text{oim/oim(heterozygous mutant)}$$

$$\#2 = \text{oim/wt(heterozygous mutant)}$$

$$\#3 = \text{wt/wt(wild type)}$$

In the above labels, "oim" indicates *osteogenesis imperfecta mutation*. The histology of similar samples were recently published that show different fibrillar structures between the three skin types.[10]

### 2.2 *Experimental Setup*

The rCSLM was performed with a confocal microscope operating in reflectance mode, in which a laser delivered light to a focus within a sample. The light reflected from this focal volume was returned to a detector through a confocal pinhole (Fig. 1). The rCSLM system in these experiments was developed for *in vivo* imaging of mouse skin, in an inverted microscope configuration (Fig. 2). The system was comprised of an argon ion laser (488-nm wavelength, 35 to 40 mW), a beamsplitter to enable delivery yet redirect reflected light to a pinhole/detector, scanning optics that consisted of *x*- and *y*-axis galvo scanning mirrors for lateral scanning at each depth of focus (Nutfield Technology, Inc. RS-15) and a pair of relay lenses for directing the scanned beams into the objective lens, an objective lens (60X water-dipping objective lens, 0.90 NA, Olympus LUMPlanFl), and a motorized *z*-axis scanning stage (Applied Scientific Instrumentation, LS50A) to move the animal for selection of the focal depth. The reflected light was redirected by the beamsplitter into a lens that focused the collimated beam through a pinhole to reach the detector. The 50-$\mu$m-diameter size of the pinhole corresponded to the central lobe of the Airy radius of the beam after magnification by the pair of relay lenses. The detector was a photomultiplier tube (Hamamatsu Photonics, 5773-01) whose voltage output was recorded by a data acquisition board (National Instruments, 6062E). The system was controlled by a laptop computer (Dell, Windows XP operating system) running a program written using Labview™ software (National Instruments). A band-rejection filter (Z488/633) was used to isolate the fluorescence signal from the reflectance signal.

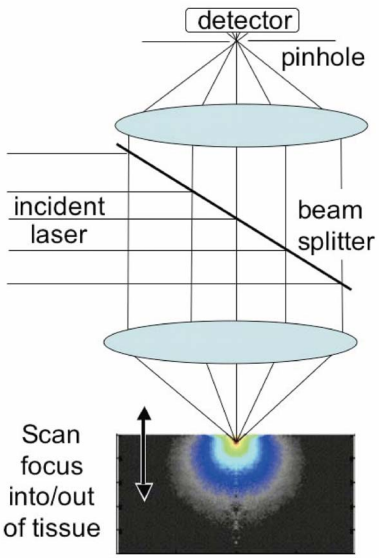


**Fig. 1** Reflectance-mode confocal measurements showing the photons scattered from the focal volume and collected by a lens that passed through a pinhole to reach the detector. The Monte Carlo simulation of fluence rate within tissue shows the glowball of diffuse light within the tissue, log(fluence rate [W/cm$^2$]), while only the tissue at the focus significantly contributes to the detected signal. The arrow shows the direction that the animal is moved to translate the focus down into the tissue.

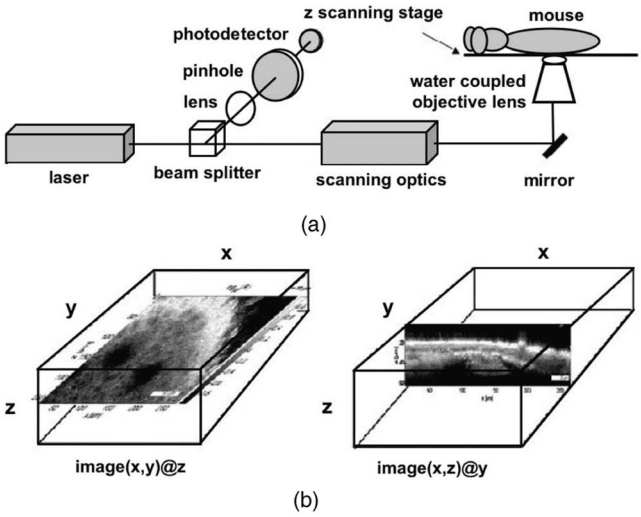


**Fig. 2** Experimental system, designed for *in vivo* imaging of mouse skin, used to image *ex vivo* skin samples in this study. (a) The inverted microscope detects reflectance from the mouse. (b) 3D images are viewed en face as image(x,y)@z or transversely as image(x,z)@y.

### 2.3 *Experimental Protocol*

The skin samples were placed epidermal surface down on a metal plate that was the size and shape of a standard microscope slide with a 2-mm-diameter hole at its center. Tissues were coupled to the objective lens through this central hole by an aqueous saline solution. The microscope viewed the skin sample from below, scanning from the epidermis up into the dermis. The $z$-axis stage stepped through 75 2-$\mu$m steps, and the $x$- and $y$-axis scanning mirrors captured a 512 $\times$512 pixel image at each depth of focus at a 25-kHz pixel acquisition rate (a rather slow acquisition in this prototype system, requiring about 10 min to complete a 3-D image). The $x,y$ pixel size was 0.50 $\mu$m$\times$0.50 $\mu$m. Experiments were conducted at a room temperature of 22 °C.

### 2.4 *Image Analysis*

A 3-D image data set, or image cube, was acquired for each of three sites on each of the two mutant samples, and on each of two sites for the wt/wt skin sample, for a total of eight image cubes. Data was recorded as $V(x,y,z)$ [Volts] in the range of 0 to 10 $V$. The pixel values for $V(z)$ were converted to reflectance units, $R(z)$ (dimensionless), by the expression

$$R = \frac{R_{og}}{V_{og}} V, \tag{1}$$

where $V_{og}$ was the measurement of an oil-glass coverslip interface, and $R_{og}$ was the value $[(n_1-n_2)/(n_1+n_2)]^2=4.056 \times 10^{-4}$, where $n_1=1.46$ (oil), and $n_2=1.52$ (glass).

For each image cube, a set of 100$\times$100 randomly chosen $x,y$ locations was analyzed. About 60% of the locations were rejected for analysis if the skin surface was not centered within the $z$-axis field of view, which would jeopardize the analysis, or if there was a hair follicle or other surface abnormality. Typically, about 4000 sites were found acceptable for analysis from each of the eight image cubes.

For each acceptable $x,y$ location, the average of 100 $R(z)$ profiles over a 10$\times$10 $x,y$ pixel (10 $\mu$m$\times$10 $\mu$m) neighborhood centered around the $x,y$ position of the chosen site was determined. The average $R(z)$ at each $x,y$ position was analyzed within the combined epidermal and papillary dermis region and the reticular dermal region of the skin to specify the exponential decays in each region. The basic equation for decay was a simple exponential decay [Fig. 3(a)] that was characterized by two parameters, $\rho$ and $\mu$, where $\rho$ was the amplitude (called reflectivity), and $\mu$ was the exponential decay constant (called attenuation). Figure 3(b) show a typical average $R(z)$ profile. The analysis found the peak reflectance associated with the stratum corneum (*sc*) to identify the front surface, then moved 10 $\mu$m deeper to find the middle of the epidermis away from the strong influence of the front surface. The papillary dermis began 25 $\mu$m deeper than the front surface, and the reticular dermis began 50 $\mu$m deeper than the front surface. The epidermis beyond 10 $\mu$m and the papillary dermis behaved similarly, and were quite variable. The typical value of attenuation $\mu$ was $\sim$100 cm$^{-1}$. The thickness of the combined epidermis and papillary dermis was $L_{\text{epi.pap}} \approx 50$ $\mu$m. Hence, the superficial attenuation by the combined epidermis and papillary dermis was $T_{\text{epi.pap}} = \exp(-\mu_{\text{epi}} L_{\text{epi}}) = \exp[-(100\ \text{cm}^{-1})(0.0050\ \text{cm})] = 0.61$. This

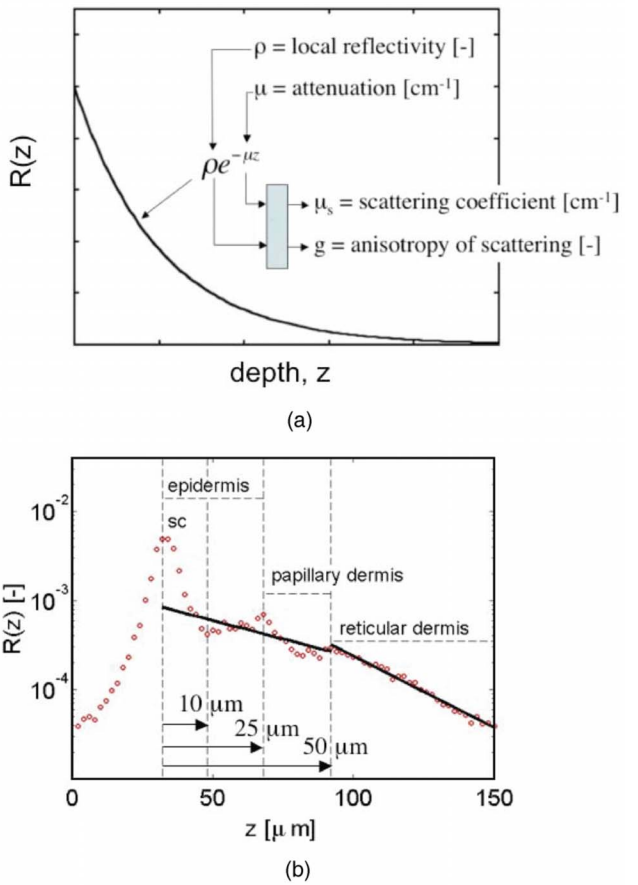


**Fig. 3** (a) As the focus of the microscope is scanned down into the tissue to a depth $z$, the reflected signal at the detector decays exponentially as $R(z)=\rho \exp(-\mu z)$. The local reflectivity, $\rho$ [dimensionless], and the attenuation, $\mu$ [cm$^{-1}$], are specified. (b) Typical axial profile $R(z)$ showing the regions associated with the stratum corneum (sc), the epidermis, the papillary dermis, and the reticular dermis. The exponential decay in the reticular dermis, after correction for the average overlying attenuation of the epidermis and papillary dermis, yielded the $\rho$ and $\mu$ of the reticular dermis, which are reported in this paper.

paper reports the results of the reticular dermis, which provided less variable data and better analysis than the papillary dermis. The reticular $\mu$ and $\rho$ were fit to the data at depths greater than 50 $\mu$m from the front surface, following the expression

$$R(z) = T_{\text{epi,pap}} \rho e^{-\mu(z-z_0)}, \tag{2}$$

where $z_0$ was the depth 50 $\mu$m from the front surface. The value of $\rho$ was the reflectivity at $z=z_0$, based on fitting the data at $z>z_0$. The average value of $T_{\text{epi.pap}}=0.61$ for all sites was used in the analysis, since attempting to use the local value of $T_{\text{epi.pap}}$ for each site introduced significant variability into the analysis. In summary, the $\rho$ and $\mu$ for the reticular dermis were determined after correcting for the average attenuation of the overlying epidermis and papillary dermis.

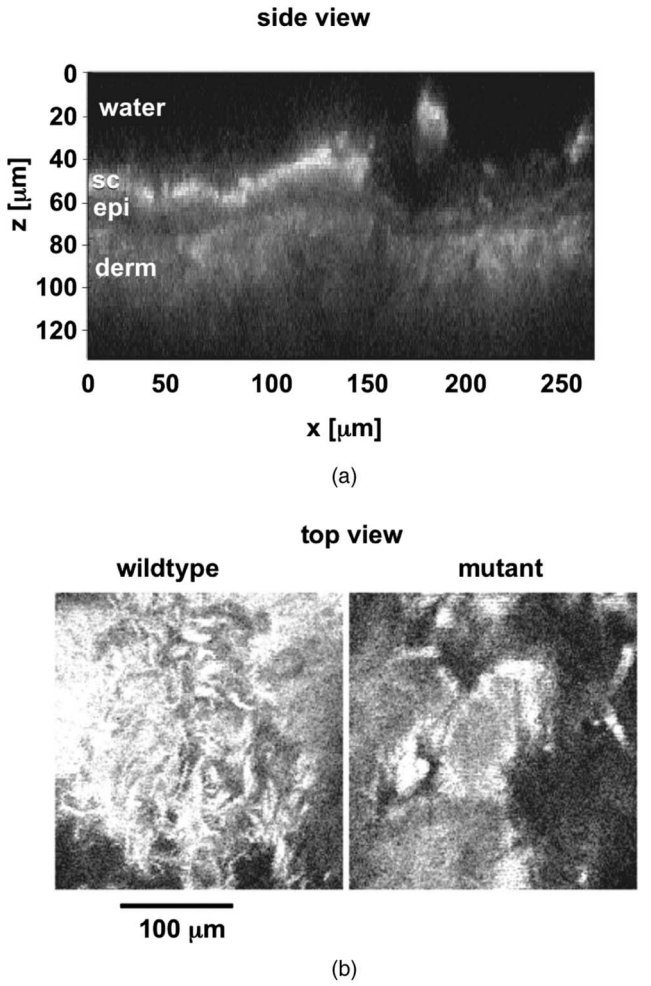


**Fig. 4** (a) Typical side view image of mouse skin (oim/oim mouse). The stratum corneum (sc), epidermis (epi), and dermis (derm) are distinguishable. The light is displayed as if incident from above through water, but experimentally the light was delivered from below. The epidermis scatters less than the water/sc boundary and the dermis. (b) Typical top view image of mouse skin, comparing a wildtype (wt/wt) on the left and a mutant (oim/oim) on the right. The wildtype presents a fibrillar appearance due to well-developed collagen fiber bundles, while the mutant presents a more homogeneous appearance. In both figures, the pixels display the logarithm of reflectance.

### 2.5 *Specifying Optical Properties*

An analysis has been developed that maps the two experimental parameters, $\rho$ and $\mu$, into the two unknown optical properties, the scattering coefficient $\mu_s$ and the anisotropy of scattering g.[5,11] The value $\rho(\mu_s, g)$ is expressed

$$\rho = \mu_s L_f b(g, NA), \tag{3}$$

where $L_f$ is the axial length of the focal volume from which light is backscattered to reach the detector through the pinhole. The product $\mu_s L_f$ gives the fraction of light delivered to the focus that is scattered by the tissue within the confocal volume. The factor $b(g, NA)$ is the fraction of the scattered light that is backscattered within the collection solid angle of the objective lens and detected at the pinhole. The value of $b(g, NA)$ is dependent on the scattering phase function $p(\theta)$, where $\theta$ is the angle of deflection of photons by the tissue, and $NA$ is the numerical aperture of the objective lens. In this work, $p(\theta)$ was specified by the Henyey-Greenstein phase function $p(g, \theta)$, which is a unique function of g that closely approximates the scattering function of skin.[12] The value $b(g, NA)$ is calculated by

$$b = \int_0^{\arcsin(NA)} p(g, \theta) 2\pi \sin(\theta) d\theta. \tag{4}$$

The value of $L_f$ is given by

$$L_f = f \frac{1.4\lambda}{NA^2}, \tag{5}$$

where $1.4\lambda / NA^2$ is the classical axial extent of the focus.[12] In these experiments, routine calibration was accomplished by imaging an oil-glass interface for use in Eq. (1). An alternative calibration used 0.1-$\mu$m-diameter polystyrene microspheres in a 2% agarose gel (150-$\mu$m thick, using glass coverslips as spacers). A collimated transmission measurement through the gel specified that $\mu_s$ equaled 96 $cm^{-1}$, which corresponded to a 0.034 volume fraction of microspheres if the microspheres behaved as predicted by Mie theory. Testing (not shown here) of sphere scattering versus sphere concentration confirmed that the spheres obeyed Mie theory at this concentration. The factor $f$ in Eq. (5) equaled 1.3, which allowed the $\mu_s$ and g predicted by Mie theory to match the experimental data. This need for a correction factor is attributed to the difficulties in using an oil-glass interface for calibration and/or to the possibility that the signal arises from a confocal volume whose axial extent exceeds the classical $L_f$. This issue is a topic of continued work, and only slightly affects the accuracy of the $\rho$ values deduced in these experiments.

The attenuation $\mu$ is also a function of $\mu_s$ and g:

$$\mu = [\mu_s a(g) + \mu_a] 2G(g, NA), \tag{6}$$

where $a(g)$ is a factor that diminishes the effectiveness of scattering to prevent photons from reaching the focus, $0 \leqslant a \leqslant 1$. The $a(g)$ depends on the forward-directed nature of the scattering events, which is a function of g. As g approaches 1, $a(g)$ approaches 0, which reduces the effectiveness of scattering in the tissue such that photons can reach the focus despite a few scattering events. The function $a(g)$ was determined by Monte Carlo simulations of photon transport to a focus within scattering media for various values of $\mu_s$ and g. The function $a(g)$ was found to follow the expression

$$a(g) = 1 - e^{-(1-g)^m/n}, \tag{7}$$

where $m = 0.6651$ and $n = 0.1555$.

The factor 2 accounts for the double path traversed by photons into and out of the tissue. The factor $G(g, NA)$ is a geometry factor that accounts for the extra pathlength the photons travel relative to the depth of focus $z$ when they are launched as a focused cone from an objective lens of numerical aperture $NA$. The value of $G(g, NA)$ is calculated by

$$G = \frac{\int_{\alpha=0}^{\arcsin(NA)} \int_{\beta=-\arcsin(NA)}^{\arcsin(NA)} \frac{1}{2}\left[\frac{z_f}{\cos(\alpha)} + \frac{z_f}{\cos(\beta)}\right] p(|\alpha-\beta|) L_{\text{arc}}(\beta) d\beta d\alpha}{\int_{\alpha=0}^{\arcsin(NA)} \int_{\beta=-\arcsin(NA)}^{\arcsin(NA)} p(|\alpha-\beta|) L_{\text{arc}}(\beta) d\beta d\alpha}, \quad (8)$$

where $z$ is the depth of the focal volume, $\alpha$ is the angle of incidence relative to the $z$ axis, $\beta$ is the angle of collection, and $L_{\text{arc}}$ is the portion of the arc of scattered light that falls within the numerical aperture of the lens. The term $p(\theta)$, where $\theta=|\alpha-\beta|$, is the Henyey-Greenstein scattering function. The term $G$ was only weakly affected by the anisotropy of the scattering function. The value of $G$ for g=0.90 was 1.37, which was used in the analysis. The value of $\mu_a$ for murine skin samples at a 488-nm wavelength was negligible; for example, a value of $\mu_a$=0.1 cm$^{-1}$ in the analysis yielded an attenuation of $\exp[-(0.1\ \text{cm}^{-1})(0.0025\ \text{cm})(2)(1.47)]=0.9995$. Experiments on the system (not shown here) showed that the signal due to autofluorescence from the skin collected in the separate fluorescence channel in the spectral range of 500 to 610 nm was 3 orders of magnitude less than the reflectance signal. Thus, the contribution of autofluorescence was not considered in the above analysis.

By using the above equations, the values of $\rho$ and $\mu$ for different values of $\mu_s$ and g were calculated and plotted as a grid on the $\rho$ versus $\mu$ graph (shown in Fig. 5). The experimentally determined data pair, $\rho$ and $\mu$, was also plotted and could be compared with the grid to specify the corresponding $\mu_s$ and g for each data pair. The magnitude of $\mu_s$ based on the confocal measurement of the spheres in gel matched the magnitude of $\mu_s$ specified by the separate collimated transmission measurement. In this manner, the method and analysis were calibrated.

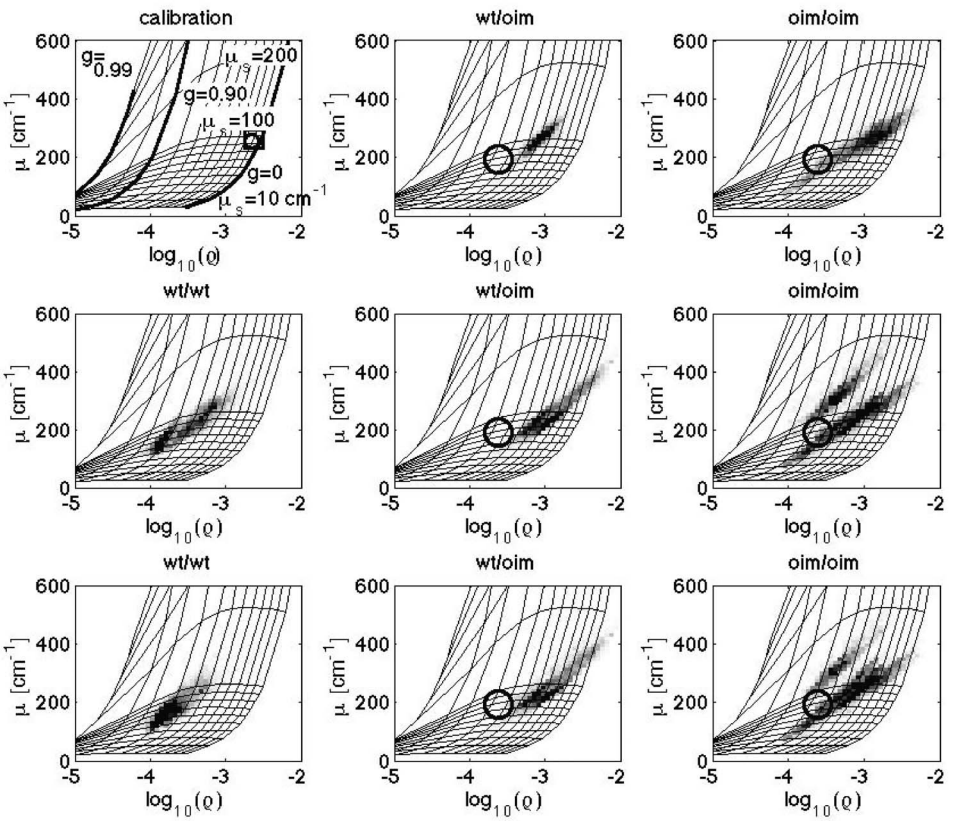


**Fig. 5** Plot of the experimentally determined $\mu$ and $\rho$ data pairs superimposed on a grid of predicted values of $\mu$ and $\rho$ for different values of $\mu_s$ and g. The distribution of data pairs for skin samples is represented by the grayscale 2-D histogram of $\mu$ versus $\rho$. The left panel shows the wildtype (wt/wt). The mean wildtype values are shown as circles in the center and right panels for reference. The center and right panels are the heterozygous mutants (wt/oim) and homozygous mutants (oim/oim), respectively. The data show a shift to the upper right toward lower g values and slightly higher $\mu_s$ values due to the mutation. The upper left panel shows the calibration and the labels for the other panels. The calibration using a confocal measurement of polystyrene microspheres (0.1-$\mu$m diameter, 0.034 volume fraction; solid circle) and a collimated transmission measurement (open square) are shown, and compare well. The grid is aligned with the confocal measurement of the microspheres.

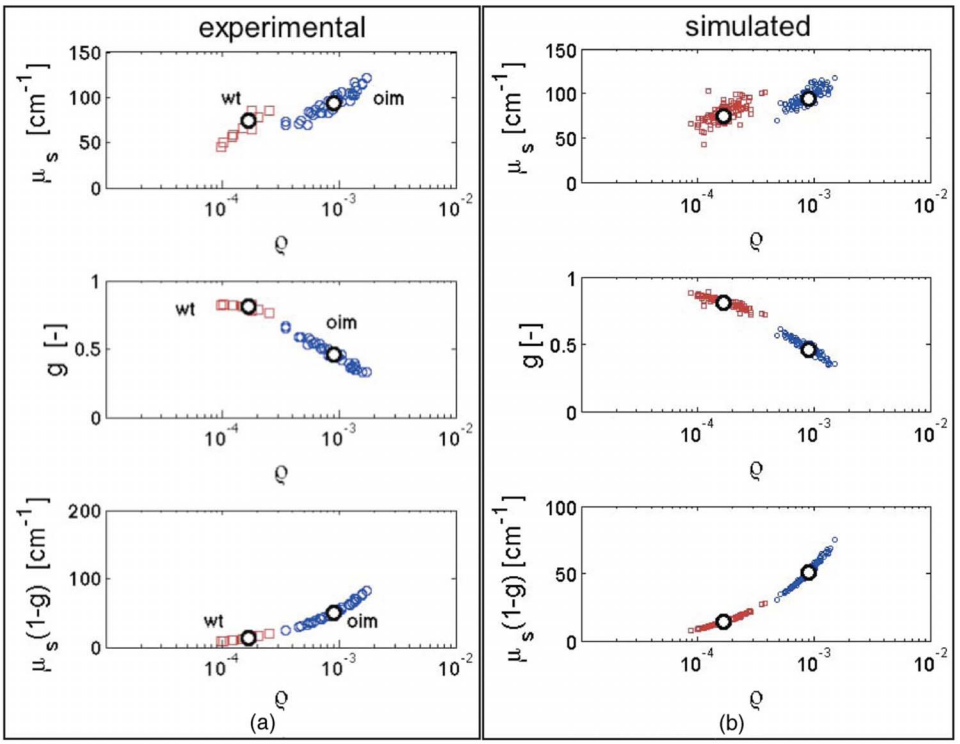


**Fig. 6** Effect of tissue variation on analysis. (a) Experimental data showing the scattering coefficient $\mu_s$ [cm$^{-1}$], anisotropy of scattering g [dimensionless], and the reduced scattering coefficient $\mu_s(1-g)$ [cm$^{-1}$] plotted versus the reflectivity $\rho$. The mutant (red squares) and oim data (blue circles) were sampled from Fig. 5. The central black circle in each data set is the approximate peak of distributed data. (b) Simulated data centered around the same peaks in the data but with random ±40% variation introduced into the function log[$R(z)$] prior to analysis to simulate the fluctuation in optical density of the skin. The spread of the simulated and experimental data is similar, suggesting that the apparent coordinate variation in the $\mu$ and $\rho$ data in Fig. 5 is the expected response to local fluctuations in the optical density of the tissue. (Color online only.)

## 3 Results

Figure 4(a) shows a typical image of a murine skin, portrayed as a cross-sectional view of $\log_{10}[R(z,x)@y]$ from the skin sample, a homozygous mutant. The various layers of the skin are labeled. The reflectance is plotted using a colorbar based on the $\log_{10}(R)$. The water/stratum corneum interface shows brightly, the epidermis has a lower reflectance, and the dermis has a stronger reflectance than the epidermis. Between $x=150$ and 200 $\mu$m, the edge of a hair follicle is seen, which disrupts the normal planar pattern of the skin. Figure 4(b) shows an en face image $\log_{10}$[R(x,y@z)], illustrating the change in collagen fiber bundles in the mutant.

Nine plots of $\rho$ versus $\mu$ are shown in Fig. 5. Each column of three plots represents a different mouse skin sample except the upper plot in the first column, which shows the calibration and labels for the iso-$\mu_s$ and iso-g contours used in the figures. The first column shows the homozygous wildtype (wt/wt), the second column shows the heterozygous mutant (wt/oim), and the third column shows the homozygous mutant (oim/oim). Data are plotted as a grayscale encoded histogram on the grid. A dark color signifies a higher frequency of occurrence of a particular data pair. In columns 2 and 3, the mean value of the wildtype data is depicted as a circle for reference. The data lay approximately in the ranges $50<\mu_s<125$ cm$^{-1}$ and $0.3<g<0.80$. The variation in the data spreads in the plot as a coordinate increase in $\mu_s$ and a decrease in g, which is considered in Sec. 4. The value of g decreases with the presence of the *oim* mutation. The distribution of data points also seems to be narrower for the wildtype and broader for the mutant tissues. A subpopulation of values in one of the wildtype sites and several of the mutant sites is not yet understood.

The calibration plot (top left graph in Fig. 5) also plots the experimentally observed $\mu$ and $\rho$ for polystyrene microspheres at a 0.034 volume fraction (circle at $\mu_s=93$ cm$^{-1}$, $g=0.13$). The grid is designed so that the prediction of Mie theory is aligned to exactly match this experimental measurement. As a test of the calibration, the $\mu_s$ specified by the collimated transmission measurement (square) is also shown. The circle within the square indicates that the collimated transmission measurement and the confocal measurement were in close agreement.

## 4 Discussion

An interesting feature of the experimental $\mu,\rho$ data in Fig. 5 is the characteristic spread of the data, in which the $\mu_s$ and g appear to vary in a coordinate manner. To clarify the nature of this variation, a simple exercise was conducted in which the analysis was applied to simulated data with added experimental variation. This exercise is shown in Fig. 6. Figure 6(a) shows a sampling of the wildtype and mutant data in the most dense portions of the histograms in Fig. 5, replotted as $\mu_s$, g, and $\mu_s(1-g)$ versus the reflectivity $\rho$. The values of $\mu_s$ and g

for the wildtype were 74 $cm^{-1}$ and 0.81, respectively. For the mutants, the values were 94 $cm^{-1}$ and 0.46. As $\mu_s$ increased, $\rho$ increased. As g decreased and $(1-g)$ increased, $\rho$ increased. As $\mu_s$ and $(1-g)$ increased—and therefore $\mu_s(1-g)$ increased—$\rho$ increased. All these results were expected, but the coordinate variation in the $x$ and $y$ values of these plots was also apparent. The central thick circles show the approximate peaks of the histograms for the wildtype and mutant. Figure 6(b) shows simulated data using the peak values of $\mu_s$ and g cited above for the wildtype and mutant. These $\mu_s$ and g values were used in Eqs. (3) and (6) to yield $\mu$ and $\rho$, then used in Eq. (2) to yield $R(z)$. Then variation was added to $R(z)$, $R(z) \leftarrow \exp\{\log[R(z)(1+\mathrm{err})]\}$ where $\mathrm{err}=(2RND-1)\times(0.40)$, and $RND$ is a vector of random numbers between 0 and 1 such that each $R(z)$ position received its own unique fluctuation. This procedure added $\pm 40\%$ variation to the simulated values of $\log[R(z)]$. Such variation may simulate variation in the optical properties of the tissue or noise imposed by laser speckle. Finally, the $\log[R(z)(1+\mathrm{err})]$ versus $z$ was fit by a straight line with $y$-intercept $\log(\rho)$ and slope $-\mu$. The resulting $\rho$ and $\mu$ were converted to $\mu_s$ and g using the analysis grid shown in Fig. 5, and the values $\mu_s(1-g)$ were calculated. This procedure yielded Fig. 6(b). The variation in the simulated results with added variation appeared similar to the variation seen in the experimental results. The source of variation is an ongoing topic of investigation.

From the data summarized in Fig. 6, the *oim* mutation appeared to decrease the anisotropy of scattering of the skin tissue from 0.81 to 0.46, which corresponds to less forward-directed scattering, presumably due to the failure of fibrils to aggregate into fiber bundles as large as the wildtype. The smaller size scale of the collagen fibers yielded more isotropic scattering. The scattering coefficient itself was only slightly increased by the mutation, from 74 to 94 $cm^{-1}$.

In summary, the rCSLM images allowed an assessment of the optical consequences of a single mutation that affected the collagen fibril assembly. The mutation caused a decrease in anisotropy g, with only a slight increase in the scattering coefficient $\mu_s$. The distinct changes in $\mu_s$ and g could be separately determined. The behavior of an ensemble of local sites could be documented, and the statistical variation encountered could be considered.

This work is preliminary in nature. These are our first studies with these wildtype and mutant skin samples. More work is needed before drawing firm conclusions about the effects of the mutant. However, this study illustrates the utility of the method and some of the considerations in applying the analysis.

## References


1. W. Cheong, S. Prahl, and A. Welch, "A review of the optical properties of biological tissues," *IEEE J. Quantum Electron.* **26**(12), 2166–2185 (1990).
2. B. C. Wilson and S. L. Jacques, "Optical reflectance and transmission of tissues: principles and applications," *IEEE J. Quantum Electron.* **26**(12), 2186–2199 (1990).
3. S. Lin, L. Wang, S. Jacques, and F. Tittel, "Measurement of tissue optical properties using oblique incidence optical fiber reflectometry," *Appl. Opt.* **36**(1), 136–143 (1997).
4. T. Collier, M. Follen, A. Malpica, and R. Richards-Kortum, "Sources of scattering in cervical tissue: determination of the scattering coefficient by confocal microscopy," *Appl. Opt.* **44**(11), 2072–2081 (2005).
5. S. Jacques, R. Samatham, N. Choudhury, and D. S. Gareau, "Specifying tissue optical properties using axial dependence of confocal reflectance images: confocal scanning laser microscopy and optical coherence tomography," *Proc. SPIE* **6446**, 64460N (2007).
6. S. L. Jacques, R. Samatham, N. Choudhury, Y. Fu, and D. Levitz, "Measuring tissue optical properties *in vivo* using reflectance-mode confocal microscopy and OCT," *Proc. SPIE* **6864**, 10 (2008).
7. D. Levitz, L. Thrane, M. H. Frosz, P. E. Andersen, C. B. Andersen, J. Valanciunaite, J. Swartling, S. Andersson-Engels, and P. R. Hansen, "Determination of optical scattering properties of highly-scattering media from optical coherence tomography images," *Opt. Express* **12**(2), 249–259 (2004).
8. D. J. Faber, F. J. van der Meer, M. C. G. Aalders, and T. G. van Leeuwen, "Quantitative measurement of attenuation coefficients of weakly scattering media using optical coherence tomography," *Opt. Express* **12**(19), 4353–4365 (2004).
9. A. Forlino and J. C. Marini, "Osteogenesis imperfecta: prospects for molecular therapeutics," *Mol. Genet. Metab.* **71**, 225–232 (2000).
10. O. Nadiarnykh, S. Plotnikov, W. A. Mohler, I. Kalajzic, D. Redford-Badwal, and P. J. Campagnola, "Second harmonic generation imaging microscopy studies of osteogenesis imperfecta," *J. Biomed. Opt.* **12**, 051805 (2007).
11. S. L. Jacques, C. A. Alter, and S. A. Prahl, "Angular dependence of HeNe laser light scattering by human dermis," *Lasers Life Sci.* **1**, 309–334 (1987).
12. M. Rajadhyaksha and S. Gonzalez, "Real-time *in vivo* confocal fluorescence microscopy," Chapter 5 in *Handbook of Biomedical Fluorescence*, M. A. Mycek and B. Pogue, eds., pp. 143–218, Marcel Decker, New York (2003).